Research Article

Haiyun Fan#, Pengying Jia#, Hailei Zhang*, Zhiyi Su, Xinwu Ba, and Yonggang Wu*

Pyrene-functionalized halloysite nanotubes for simultaneously detecting and separating Hg(II) in aqueous media: A comprehensive comparison on interparticle and intraparticle excimers

https://doi.org/10.1515/ntrev-2022-0119
received March 2, 2022; accepted April 27, 2022

Abstract: The development of a facile approach to simultaneously detect and separate Hg(II) ions in an aqueous solution is a challenging topic in the chemosensing field. Herein, we focus on constructing the Hg(II)-sensitive fluorescence "turn-on"-type composite materials by using halloysite nanotube (HNT) as substrate. Two types of HNTs-based chemosensors, HNTs-PHT and HNTs-BP, were developed in this study, which exhibit Hg(II)-sensitive fluorescence "turn on" behavior by forming interparticle and intraparticle excimers, respectively. Fortunately, HNTs-PHT is able to effectively restrict the solvent relaxation of π–π* transition and make it a better detection tool in aqueous solution than HNTs-BP. The addition of Hg(II) can trigger a dramatical increase at 469 nm in emission curves of HNTs-PHT, which cannot exhibit emission behaviors without the addition of Hg (II). Furthermore, the formation of interparticle excimers makes Hg(II) serve as a crosslinker to aggregate HNTs-PHT into precipitations. Following this way, Hg(II) ions can be facilely removed from the water *via* a simple filtration or centrifugation approach. The as-prepared HNTs-PHT shows high specificity and precision in simultaneously detecting and separating Hg(II) without the recourse to energy consumption, which will give a novel insight to deal with heavy metal pollution.

Keywords: halloysite nanotube, pyrene, clay, chemosensor, Hg(II)

1 Introduction

The exceeded hazard of metal salts, especially the heavy metal ions in water, is an increasingly serious problem in the environmental protection field around the world in recent years [1,2]. The nonbiodegradable nature, bioaccumulation, and high toxicity give rise to severe health risks for humans [3,4]. Among the various heavy transition metals, mercury (Hg) is serving as the main role in heavy metal pollution, which has been reported to be usually involved in wastewater [5]. It should be noted that Hg is highly toxic that even 10^{-6} M can also result in irretrievable damages to health, even death [6,7]. A prime challenge for researchers is, therefore, to develop a facile, versatile, specific and sensitive system for simultaneous detection and separation of Hg(II) ions in water.

Up to now, some analytical methods have been built for detecting Hg(II) ions, including localized surface plasmon resonance (LSPR) [8], high-performance liquid chromatography (HPLC) [9] and electrochemistry technique [10,11]. The fluorescence-based method shows promising advantages including naked eye visualization capability, high selectivity and facile operation when used in the detection of metal ions [12,13]. It is worth noting that planar-conjugated molecules, the main source of fluorescent chromophores, often show poor water solubility and aggregate to form π–π accumulations in water [14]. So, some unexpected phenomena usually take place when dissolving or dispersing the planar-conjugated molecules in water, *e.g.* aggregation-caused quenching, formation of excimers, large fluctuation in fluorescence intensity, and poor reproducibility [15,16]. At present, the use of planar-conjugated molecules as

# These authors contributed equally to this work.

*** Corresponding author: Hailei Zhang,** College of Chemistry & Environmental Science, Hebei University, Baoding, 071002, China, e-mail: zhanghailei@hbu.edu.cn
*** Corresponding author: Yonggang Wu,** College of Chemistry & Environmental Science, Hebei University, Baoding, 071002, China, e-mail: wuyonggang@hbu.edu.cn
Haiyun Fan, Pengying Jia, Zhiyi Su, Xinwu Ba: College of Chemistry & Environmental Science, Hebei University, Baoding, 071002, China

detection tools is mainly limited to organic solvents or mixing solvents. Very few cases can be used in the pure water phase, which seriously reduces their practical application level. Functionalization of the planar-conjugated molecules with hydrophilic groups can improve the water solubility but may be not effective to solve the solvent relaxation problems of π–π* transition in water. The amphipathic molecules are easy to form micelles and also contribute to the unexpected influence on fluorescence behaviors [17,18]. These problems inspired us to explore novel detection systems with good feasibility in water.

There are some studies reported in the literature regarding Hg(II) detection and removal based on physically immobilizing organic ligands onto nanomaterials aiming to meet the application in an aqueous solution [19,20]. However, the physical immobilization usually suffers from serious stability problems. Our hypothesis is to covalently functionalize the chemosensor on the surface of nanoparticles with good water dispersion and surface charge repulsion [21], which is quite beneficial to overcome the stability problems in physically immobilized nanocomposites.

In this way, the self-aggregation behavior and solvent relaxation of the π–π* transition can be effectively suppressed. Otherwise, the formation of interparticle excimers makes the Hg(II) ions act as crosslinking points and drive the nanoparticles into precipitation, meeting the requirement of Hg(II) separation. Halloysite nanotube (HNT) [22,23], a natural tubular nanomaterial, was selected as the substrate for the construction of the smart tool for simultaneous detection and separation of Hg(II) ions. Benefiting from the hollow tubular structure, HNTs exhibit lower relative density and thereby better water dispersion than other commonly used nanoparticles such as silica [24,25]. The self-aggregation behavior, usually taking place in nanoparticles, is effectively suppressed based on the external charge distribution [26]. Other favorable merits including good biocompatibility [27,28], nontoxicity [29], non-degradation [30], hydrophilic [31] and low-cost [32] also make HNTs promising materials in the field of environmental protection [33–36], biomaterial [37–40], catalyst [41–43], battery [44], sensor [45,46], and coating [47]. Herein, the HNTs-based smart tool for the simultaneous detection and separation of Hg(II) ions was facilely developed by anchoring the pyrene-containing chemosensor on the surface of HNTs, which exhibit an obvious "turn on" response on fluorescence after the addition of Hg(II) in water. Moreover, the Hg(II)-chelated aggregation would enlarge the particle sizes and result in macroscopic precipitations, which can serve as a facile separation approach without the recourse to energy consumption. As a result, a smart tool for simultaneously detecting and separating Hg(II) in aqueous media was developed, which may pave a new path for managing metal ions not merely Hg(II). Further studies will focus on exploiting more HNT-based detection systems with more simplified processes.

2 Experimental

2.1 Materials

HNTs were obtained from GuangZhou Shinshi Metallurgy and Chemical Co., Ltd., and purified before use [48]. Aminated HNTs (HNTs-NH_2) and acyl chloride-bearing HNTs (HNTs-COCl) were prepared according to our previous work [49,50]. 4-Bromothiophene-2-carbaldehyde (A1), hydrazine hydrate, *o*-nitrophenol (B1), 1,3-dibromo-2-propanol (B2), 1-pyrenealdehyde (A3) and anhydrous $SnCl_2$ in the analytical grade were purchased from Shanghai Aladdin Bio-Chem Technology Co., Ltd. 4-(Formylphenyl)boronic acid (A5) was purchased from Soochiral Chemical Science & Technology Co., Ltd. Oxalyl chloride and KH550® were obtained from Energy-Chemical.

2.2 Synthesis and preparation

2.2.1 Synthesis of A2

4-Bromothiophene-2-carbaldehyde (A1, 1.00 g, 5.24 mmol), $MgSO_4$ (1.26 g, 10.48 mmol) and hydrazine hydrate (1.00 mL) were dissolved in ethanol (30 mL) and heated at 80°C under N_2 atmosphere for 6 h. Then, the solution was cooled to room temperature and extracted three times with dichloromethane and saturated NaCl solution. After removal of the solvent in a vacuum, the residue was chromatographically purified on silica gel eluting with dichloromethane to afford A2 as a white solid (1.05 g, 98%). ^{1}H NMR (400 MHz, $CDCl_3$) δ (ppm): 7.80 (s, 1H), 7.11 (s, 1H), 6.94 (s, 1H), 5.55 (s, 2H). ^{13}C NMR (100 MHz, $CDCl_3$) δ (ppm): 181.84, 144.04, 137.97, 132.26, 111.51. MS (ESI): m/z: calcd for $C_5H_5BrN_2S$: 205.07 $[M]^+$; found: 206.86 $[M + 2H]^{+\cdot}$

2.2.2 Synthesis of A4

Compound A2 (0.70 g, 3.41 mmol), 1-pyrenealdehyde (A3, 0.86 g, 3.75 mmol) and $MgSO_4$ (0.82 g, 6.82 mmol) were dissolved in absolute ethanol (30 mL) and stirred at

80°C under N_2 atmosphere for 15 h. Then, the solution was cooled to room temperature and extracted for three times with dichloromethane and saturated NaCl solution. After removal of the solvent, the residue was chromatographically purified on silica gel eluting with petroleum ether/dichloromethane (3:1, v/v) to afford A4 as a faint yellow solid (0.98 g, 69%). ^{1}H NMR (400 MHz, d_6-DMSO) δ (ppm): 9.67 (s, 1H), 9.14 (d, J = 6.4 Hz, 1H), 9.04 (s, 1H), 8.69 (d, J = 5.6 Hz, 1H), 8.42–8.35 (m, 4H), 8.32 (d, J = 6.0 Hz, 1H), 8.25 (d, J = 6.0 Hz, 1H), 8.15 (t, J = 10.4 Hz, 1H), 7.96 (s, 1H), 7.75 (s, 1H). ^{13}C NMR (100 MHz, d_6-DMSO) δ (ppm): 161.96, 155.98, 155.60, 140.41, 140.01, 135.98, 135.82, 133.57, 131.28, 130.63, 130.42, 129.73, 129.66, 129.14, 128.91, 127.91, 127.34, 127.26, 126.97, 126.72, 126.62, 125.66, 124.60, 124.11, 123.82, 110.29. MS (ESI): m/z: calcd for $C_{22}H_{13}BrN_2S$: 417.32 $[M]^+$; found: 418.72 $[M+H]^+$.

2.2.3 Synthesis of A6

Compound A4 (0.30 g, 0.72 mmol), (4-formylphenyl)boronic acid (A5, 0.13 g, 0.86 mmol), K_2CO_3 (0.6 g, 4.34 mmol) and $Pd(PPh_3)_4$ (8 mg, 0.007 mmol) in H_2O (4 mL) and tetrahydrofuran (THF) (30 mL) were carefully degassed. The mixture was heated by microwave reactor at 65°C and stirred under N_2 atmosphere for 2.5 h. After cooling to room temperature, saturated NaCl solution and dichloromethane (2:1, v/v) were added. The organic layer was separated and then stirred with anhydrous Na_2SO_4. After filtration and removal of the solvent in vacuum, the residue was chromatographically purified on silica gel eluting with petroleum ether/dichloromethane (2:1, v/v) to afford A6 as a faint yellow solid (302 mg, 95%). ^{1}H NMR (400 MHz, d_6-DMSO) δ (ppm): 10.05 (s, 1H), 9.73 (s, 1H), 9.16 (d, J = 9.6 Hz, 1H), 9.13 (s, 1H), 8.74 (d, J = 8.4 Hz, 1H), 8.42 (m, 5H), 8.33 (s, 1H), 8.27 (d, J = 8.4 Hz, 2H), 8.17 (t, J = 15.6 Hz, 1H), 8.01 (s, 4H). MS (ESI): m/z: calcd for $C_{29}H_{18}N_2OS$: 442.54 $[M]^+$; found: 442.86 $[M]^+$; FTIR: 3,447, 3,103, 3,039, 3,955, 2,921, 2,848, 2,760, 1,918, 1,875, 1,685, 1,600, 1,308, 1,294, 1,249, 1,231, 1,225, 1,211, 1,187, 1,171, 937, 901, 849, 830, 785, 716, 681, 660, 624, 612, 547, 535, 509, 499.

2.2.4 Synthesis of B3

O-Nitrophenol (B1, 3.00 g, 21.56 mmol), 1,3-dibromo-2-propanol (B2, 1.90 g, 8.72 mmol) and KOH (3.00 g, 17.86 mmol) were dissolved in dimethyl sulfoxide (15 mL) under N_2 atmosphere. The solution was heated at 90°C for 4 h. After cooling to room temperature, the solution was extracted three times with dichloromethane and saturated NaCl solution. The organic layer was collected and then stirred with anhydrous Na_2SO_4. After filtration and removal of the solvent in a vacuum, the residue was chromatographically purified on silica gel eluting with dichloromethane to afford B3 as a faint yellow solid (85%). ^{1}H NMR (400 MHz, $CDCl_3$) δ (ppm): 7.88 (d, J = 8.0 Hz, 2H), 7.56 (t, J = 16.0 Hz, 2H), 7.16 (d, J = 8.0 Hz, 2H), 7.06 (t, J = 16.0 Hz, 2H), 4.43 (m, 2H), 4.34 (m, 2H), 3.04 (br, 1H). ^{13}C NMR (100 MHz, $CDCl_3$) δ (ppm): 151.98, 139.60, 134.73, 125.95, 121.11, 115.06, 69.56, 68.01. MS (ESI): m/z: calcd for $C_{15}H_{14}N_2O_7$: 334.28 $[M]^+$; found: 335.00 $[M+H]^+$.

2.2.5 Synthesis of B4

Compound B3 (1.50 g, 4.49 mmol) was dissolved in an ethanol/THF mixed solution (5:1, v/v) with the addition of an HCl solution containing anhydrous $SnCl_2$. The system was carefully degassed and heated at 80°C for 8 h under a nitrogen atmosphere. After cooling to room temperature, saturated NaCl solution and dichloromethane (2:1, v/v) were added. The organic layer was separated and then stirred with anhydrous Na_2SO_4. After filtration and removal of the solvent, the residue was chromatographically purified on silica gel eluting with dichloromethane to afford B4 as a brown viscous liquid (1.11 g, 90%). ^{1}H NMR (400 MHz, $CDCl_3$) δ (ppm): 6.89–6.75 (m, 8H), 4.41 (m, 1H), 4.17 (m, 4H), 3.86 (s, 5H). ^{13}C NMR (100 MHz, $CDCl_3$) δ (ppm): 148.98, 135.76, 122.02, 118.99, 115.19, 111.35, 70.02, 68.89. MS (ESI): m/z: calcd for $C_{15}H_{18}N_2O_3$: 274.32 $[M]^+$; found: 275.04 $[M+H]^+$.

2.2.6 Synthesis of B5

Compound B4 (0.60 g, 2.19 mmol), 1-pyrenealdehyde (A3, 1.11 g, 4.81 mmol) and $MgSO_4$ (3.87 g, 8.76 mmol) were dissolved in absolute ethanol (50 mL) and stirred at 80°C under N_2 atmosphere for 15 h. Then, the solution was cooled to room temperature and extracted for three times with dichloromethane and saturated NaCl solution. After removal of the solvent, the residue was chromatographically purified on silica gel eluting with petroleum ether/dichloromethane (2:1, v/v) to afford B5 as a yellow solid (0.92 g, 60%). ^{1}H NMR (400 MHz, d_6-DMSO) δ (ppm): 9.52 (s, 2H), 9.27 (d, J = 9.2 Hz, 2H), 8.64 (d, J = 8.0 Hz, 2H), 8.36 (d, J = 7.6 Hz, 2H), 8.28 (d, J = 7.6 Hz, 6H), 8.20–8.16 (m, 4H), 8.10 (t, J = 15.2 Hz, 2H), 7.28 (d, J = 9.2 Hz, 2H), 7.11–6.99 (m, 6H), 5.47 (d, J = 4.0 Hz, 1H), 4.35–4.26 (m, 5H). ^{13}C NMR (100 MHz, d_6-DMSO) δ (ppm): 163.65, 155.25, 144.64, 134.36, 131.24, 130.24, 129.40, 129.33, 129.03, 127.86, 127.65, 127.03, 126.68, 126.35, 125.40, 124.51, 124.13, 123.77,

122.33, 121.62, 116.86, 116.24, 115.27, 72.90, 68.33. MS (ESI): *m*/*z*: calcd for $C_{49}H_{34}N_2O_3$: 698.82 $[M]^+$; found: 698.49 $[M]^+$; FTIR: 3,351, 3,044, 2,923, 2,868, 1,922, 1,801, 1,674, 1,610, 1,595, 1,579, 1,538, 1,506, 1,486, 1,448, 1,382, 1,241, 1,188, 1,111, 1,033, 898, 847, 819, 747, 712, 679, 607.

2.2.7 Preparation of HNTs-PHT

Compound A6 (80 mg, 0.18 mmol) and anhydrous $MgSO_4$ (65 mg, 0.54 mmol) were dissolved into 20 mL of ethanol. Then, 200 mg of HNTs-NH_2 was added to the solution. The mixture was refluxed for 8 h and then centrifuged to collect the residue. The residue was purified by washing with water, ethanol and dichloromethane. After drying in a vacuum, the pyrene-functionalized product HNTs-PHT was achieved as a yellow solid (160 mg).

2.2.8 Preparation of HNTs-BP

HNTs-COCl (270 mg), compound B5 (80 mg) and triethylamine (800 μL) in 5 mL of DMSO were vigorously stirred at 50°C under an N_2 atmosphere. After cooling to ambient temperature, the suspension was centrifuged to collect the residue. The residue was then purified by washing with water and ethanol. After drying in a vacuum, the bispyrene-containing product HNTs-PB was achieved as a yellow solid (260 mg).

2.3 Characterizations

Transmission electron microscopy (TEM) observations and energy-dispersive spectrometer (EDS) mapping were performed on a field emission transmission electron microscope (Tecnai G2 F20 S-TWIN, FEI). Attenuated total refraction FTIR spectra were recorded on a Thermo Fisher Scientific NICOTET IS10 FTIR spectrophotometer in the region of 4,000–400 cm^{-1}. NMR data were recorded on a WNMR spectrometer or a Bruker Advance III spectrometer (400 MHz). X-ray photoelectron spectroscopy (XPS) data were collected *via* a Thermo Scientific ESCALab 250Xi XPS equipped with 200 W monochromated Al Ka radiation. Thermogravimetric analysis (TGA) was performed on a Pyris1 TGA instrument under the nitrogen atmosphere. MS analyses were obtained by using a Bruker Daltonics Autoflex III. Turbidity test and fluorescence experiments were conducted on a Shimadzu UV-Vis spectrometer model UV-2550 and a Shimadzu RF-5301PC photometer, respectively.

3 Results and discussion

3.1 Synthesis and structural characterization

Two types of HNTs-based chemosensors were developed for simultaneously detecting and separating Hg(II) ions (Scheme 1). As for Type I, HNTs-PHT was prepared by anchoring aldehyde-containing pyrene derivative (A6) on the surface of aminated HNTs (HNTs-NH_2) *via* a typical Schiff base reaction, in which "P" represents "pyrene," "H" represents "hydrazone" and "T" represents thiophene. The pyrene–hydrazone–thiophene moiety in obtained HNTs-PHT can serve as an ionophore to Hg(II) ion and trigger a "turn on" fluorescence by the formation of interparticle excimer. As for the other type of HNTs-based chemosensor, HNTs-BP was synthesized by treating acyl chloride-bearing HNTs (HNTs-COCl) with bispyrene-based chemosensor (B5) *via* the reaction between –COCl and –OH groups, in which the "BP" is abbreviated for bispyrene. The nitrogen and oxygen atoms in the backbone of B5 moiety are able to chelate with Hg(II) ions with the formation of intraparticle excimer. The reactants were kept in high concentrations in the above-mentioned Schiff base reaction and esterification reaction aiming to afford desirable grafting degrees. The as-obtained HNTs-PHT and HNTs-BP were carefully characterized by FTIR, TGA, solid-state NMR and XPS.

The FTIR spectrum of HNTs features three distinct peaks at 3,701, 3,625 and 1,030 cm^{-1} in Figure S18. The stretching vibration around 1,030 cm^{-1} should be attributed to the in-plane Si–O–Si. Owing to the curly and multilayer character of HNTs, the Al–OH groups are categorized into two different kinds. As a result, the band in the FTIR spectrum of HNTs divides into two peaks. The peak at 3,701 cm^{-1} should be attributed to the stretching vibrations of Al–OH on the lumen surface, meanwhile, the peak at 3,625 cm^{-1} can be ascribed to the Al–OH groups inside the multilayered structure. It should be noted that the peaks assigned to Al–OH groups and Si–O–Si groups can also be detected after the amination approach, Schiff base reaction and esterification reaction, suggesting that the aluminosilicate composites did not undergo serious damage in the modification processes.

^{13}C solid-state NMR spectra of HNTs-PHT and HNTs-BP are shown in Figure 1, in which the peaks have been completed and interpreted. Original HNTs cannot display signals in the ^{13}C solid-state NMR spectrum, which has been evidenced in our previous study [51]. So, the peaks in HNTs-PHT and HNTs-BP should be caused by the carbons in A6 and B5 moieties, respectively. As for HNTs-PHT, the carbons

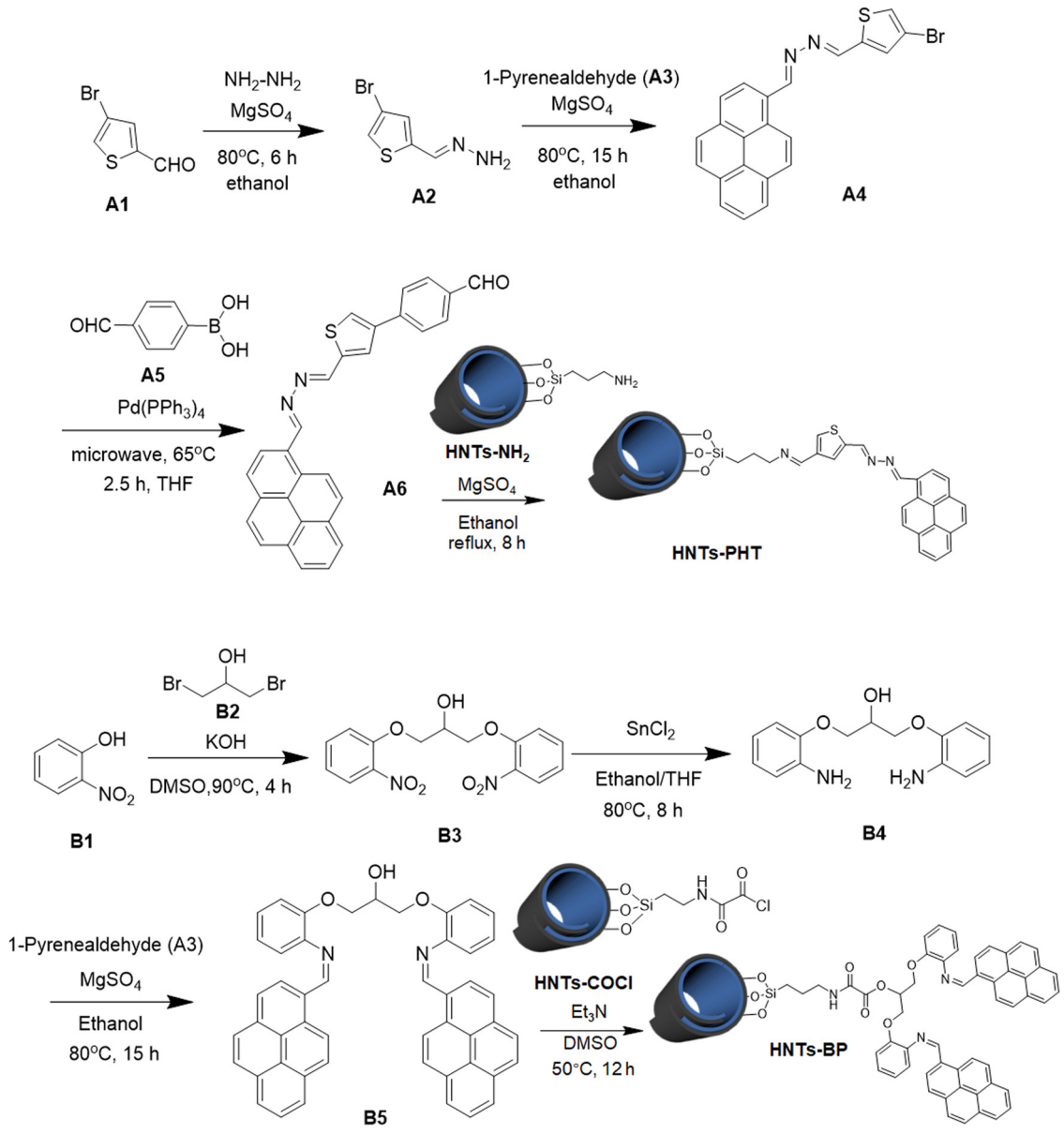

Scheme 1: Synthetic approaches to HNTs-PHT and HNTs-BP.

in –C═N– units give the signals in high-frequency regions, *e.g.* 159.90 and 148.46 ppm. The strong peaks located at 131.11, 128.27 and 122.38 ppm should be assigned to the carbons in pyrene groups and partly carbons in thiophene moiety. The peaks less than 40 ppm should be attributed to the carbons in saturated alkyl chains. The ^{13}C solid-state NMR spectrum of HNTs-BP also displays the peaks at 159.42, 153.86, 14.54, 128.75, 124.47 and 108.88 ppm, which should be assigned to carbons in unsaturated groups, including benzene unit and pyrene groups. The weak peak at 64.01 ppm is caused by the carbons in saturated units near oxygen atoms. The NMR results match well with the ^{13}C NMR data in Figure S11.

To further reveal the composition of HNTs-PHT and HNTs-BP, XPS analyses were conducted and are summarized in Figure 2. Figure 2a shows the XPS curves of HNTs, HNTs-PHT and HNTs-BP. The XPS spectrum of original HNTs shows the existence of aluminum (Al 2s and Al 2p) and silicon (Si 2s and Si 2p) in the range from 154 to 75 eV, matching well with the components in aluminosilicate clays. The strongest peak can be found at 532 eV, which should be assigned to O 1s signal. Regions from 290 to 280 eV relating to C 1s are expanded in Figure 2b. Original HNTs display a weak C 1s signal, which may be caused by the naturally curly process. HNTs-PHT and HNTs-BP show much stronger intensity for the C 1s peak at 284.8,

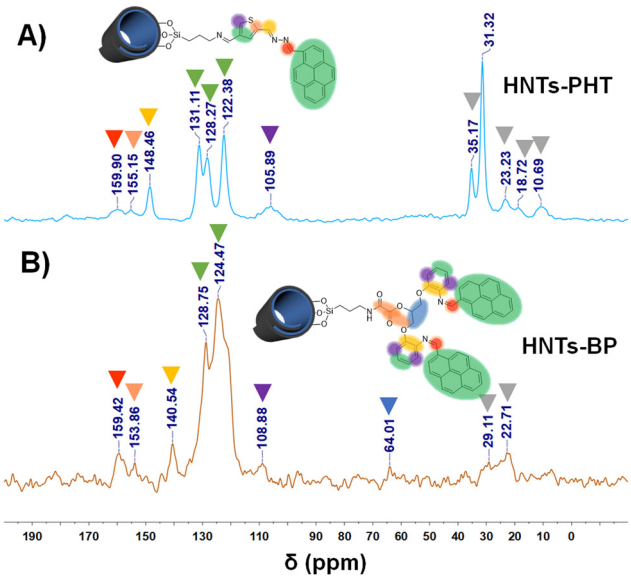

Figure 1: ^{13}C solid-state NMR spectra of HNTs-PHT (a) and HNTs-BP (b).

which should be attributed to the anchoring of the chemosensors onto the HNTs. The presence of unsaturated groups contributes to the peaks around 288.5 eV.

Figure 2c shows the expanded regions from 411 to 394 eV relating to N 1s regions. The N 1s signal is undetected in original HNTs. Because of the presence of nitrogen in A6 and B5 moieties, both HNTs-PHT and HNTs-BP display N 1s peaks in the XPS curves. The difference in peak value and peak pattern can be clearly found between HNTs-PHT and HNTs-BP. As for HNTs-BP, nitrogen can be found in –NH– and –N═C– groups. The presence of –C═N–N═C– gives rise to a more complex peak pattern in HNTs-PHT. Moreover, the presence of S can be evidenced by the S 2p peak at 164.1 eV in Figure 2d. The XPS observations, as well as NMR findings, are in agreement with the expected structures of HNTs-PHT and HNTs-BP. Furthermore, the grafting degrees were calculated from the TGA curves depicted in Figure 3. The grafting degrees are 6.2, 9.2 and 9.8% for HNTs-NH_2, HNTs-PHT and HNTs-BP, respectively.

3.2 Optical properties and the detection properties upon Hg(II)

The fluorescent emission behavior of HNTs-BP was evaluated in water, which displayed an unexpected emission peak at 469 nm (Figure 4a) with the fluorescence quantum yield (Φ) at 0.06. Pyrene usually displays its emission peak at ca. 430 nm, while the emission peak of 469 nm should be attributed to the solvent effect rather than the monomer emission. Generally, pyrene is very sensitive to the polarity of the solvent [52,53]. In nonpolar solvents, *e.g.* THF and CH_2Cl_2, the fluorescence signal originates from pyrene only for monomer emission. In addition to the monomer emission, the formation of intense excimer emission can take place in polar solvents, due to the solvent relaxation of the π–π* transition. Hence, the titration of HNTs-BP with polarity was conducted by preparing the stock solution of HNTs-BP in only THF and, then, varying the water concentration from 0 to 90%. HNTs-BP does not show any excimer emission in only THF solvent (Figure S20). With the gradual addition of water, the fluorescence intensity increases significantly with obvious bathochromic shifts. The results show that the intramolecular rotation of the pyrene platform is restricted, which results in the formation of excimers without recourse to Hg(II). After the addition of Hg(II), the fluorescence intensity at 469 nm was increased by ca. 2-fold without any bathochromic or hypsochromic shift, in which the Φ increased to 0.09. In this case, Hg(II) can chelate with N and O atoms in HNTs-BP and force the pyrene platform to form more excimers (Figure 4b). However, the strong background fluorescent emission and the inconspicuous difference in fluorescence intensity make HNTs-BP not a desirable detection tool for Hg(II).

For the other case, when HNTs-PHT dispersed into water, non-fluorescent emission behavior can be observed ($\Phi < 0.001$) (iii in Figure 4c). The solvent relaxation of the π–π* transition was effectively reduced. The N and S atoms in HNTs-PHT are able to chelate with Hg(II) and force the pyrene moieties to afford interparticle excimers, which can cause a dramatical enhancement of fluorescence. Following this way, a remarkable fluorescence "turn on" behavior from nonfluorescent to strong fluorescent (iv in Figure 4c) can be found with the addition of Hg(II) with an increased Φ value at 0.07. The remarkable fluorescence enhancement at 469 nm matches well with the proposed mechanism in Figure 4d. As a result, HNTs-PHT shows a much better detection performance in an aqueous solution than HNTs-BP.

To evaluate the detection accuracy and sensitivity of HNTs-PHT to Hg(II), an aqueous solution with different quantities of Hg(II) was added to HNTs-PHT aqueous suspension to reveal the relationship between fluorescence intensity and the concentration of Hg(II). Plot of fluorescence intensity (I_x) of HNTs-BP aqueous suspension *vs* the concentration of Hg(II) ([Hg(II)]) was recorded. The fitting results indicate that the linear regression for I_x and [Hg(II)] exhibit a good linear correlation coefficient ($R > 0.99$). A good linearity relationship was achieved within the range from 1.0×10^{-5} to 1.0×10^{-4} M (Figure S21).

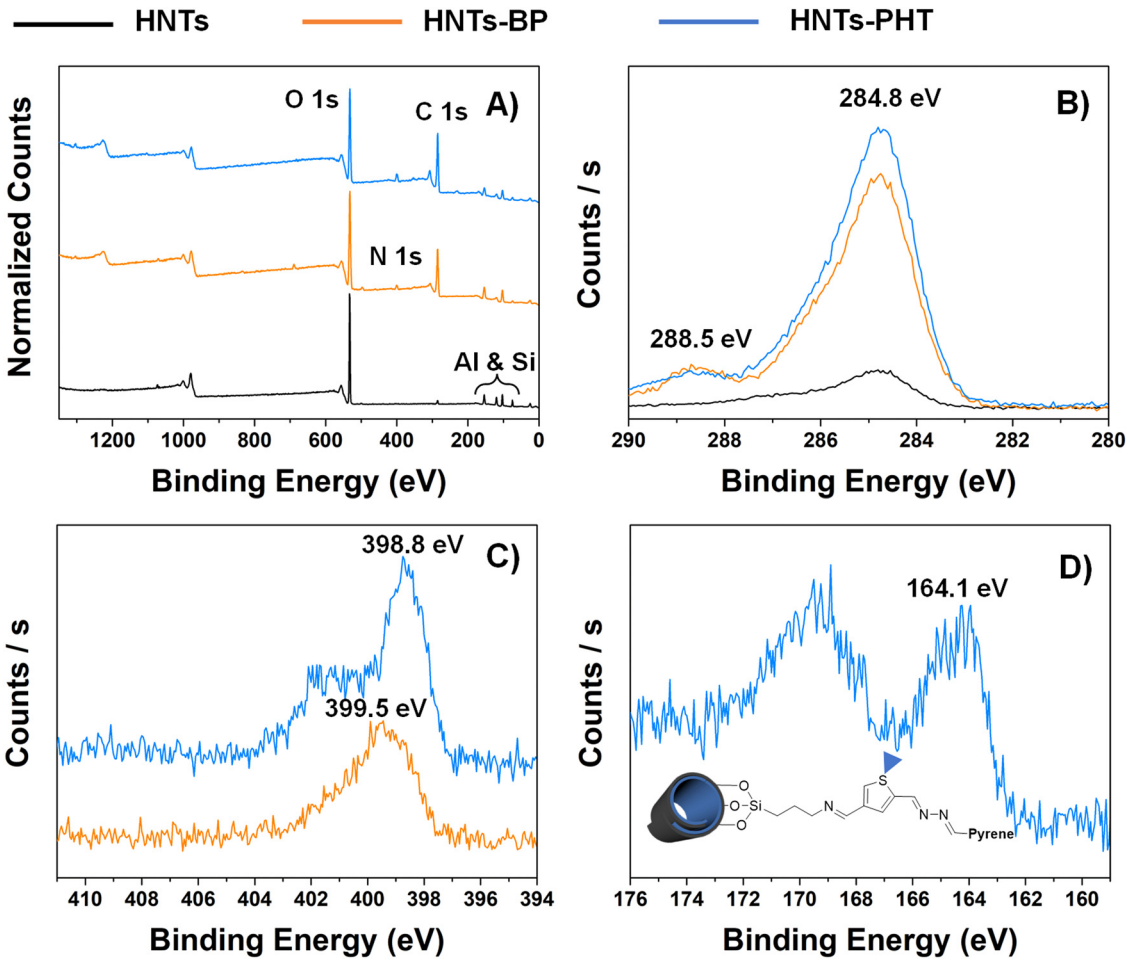

Figure 2: XPS studies [(a) XPS curves of HNTs, HNTs-PHT and HNTs-BP; (b) C 1s regions of HNTs-PHT and HNTs-BP; (c) N 1s regions of HNTs-PHT and HNTs-BP; and (d) S 2p regions of HNTs-PHT].

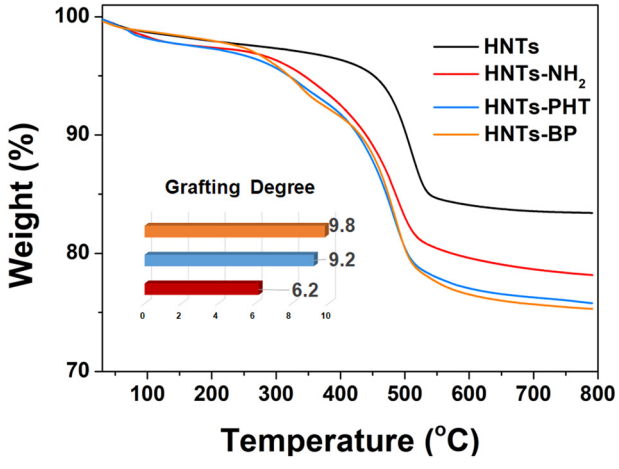

Figure 3: TGA curves of HNTs, HNTs-NH_2, HNTs-PHT and HNTs-BP.

Some studies have shown that some other metal ions are also able to chelate with O, N or S atoms [54–57]. Therefore, the specificity of HNTs-PHT to Hg(II) over commonly used ions, including Zn^{2+}, Pb^{2+}, Ni^{+}, Na^{+}, Mn^{2+}, Mg^{2+}, K^{+}, Fe^{2+}, Cu^{2+}, Ba^{2+} and Al^{3+}, was also investigated (the concentration is equal to 1×10^{-5} M, details are shown in Figure 5). Upon individual addition of a wide range of the abovementioned metal ions as their SO_4^{2-} or Cl^{-} salts, only Hg(II) raised a conspicuous fluorescence enhancement at 469 nm with the I_x value higher than 1,800 a.u. The fluorescence ratio "*r*" of the fluorescence intensity at 469 nm with and without the addition of ion was employed to evaluate the specificity upon Hg(II). Except for Hg(II), the *r*-value was found less than 5.0 for all cases. The addition of Hg(II) raised a much higher

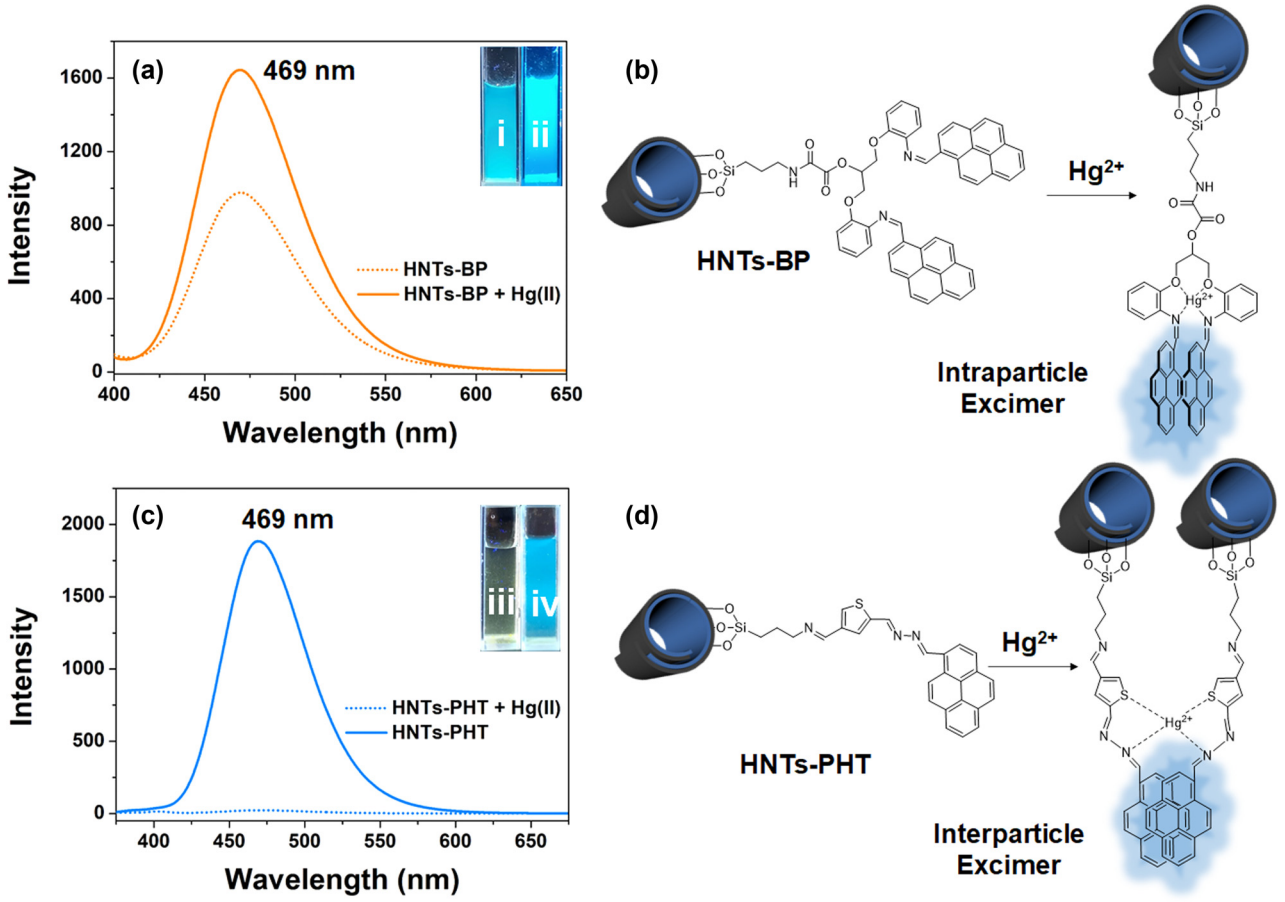

Figure 4: Study on luminescence properties. [(a) Fluorescence emission spectra of HNTs-BP with (iv) or without (iii) the addition of Hg(II); (b) mechanism of the Hg(II)-triggered intraparticle excimer in case of HNTs-BP; (c) fluorescence emission spectra of HNTs-PHT with (ii) or without (i) the addition of Hg(II); and (d) mechanism of the Hg(II)-triggered interparticle excimer in case of HNTs-PHT].

r-value at 81.88. These results indicate that the as-obtained HNTs-PHT exhibits highly specific, precise and sensitive responses to Hg(II) in an aqueous system.

3.3 Absorption studies

The absorption behaviors of HNTs-based chemosensors on Hg(II) were confirmed by TGA curves. The weight (%) at 790°C for HNTs-PHT and HNTs-BP in TGA curves is 75.8 and 75.3%, respectively. After treating with excess $Hg(ClO_4)_2$, the Hg(II)-chelated products, HNTs-PHT-Hg(II) and HNTs-BP-Hg(II), were also examined by TGA. The weight (%) at 790°C for HNTs-PHT-Hg(II) and HNTs-BP-Hg(II) in TGA curves increased to 78.2 and 77.5%, respectively, suggesting the absorption of Hg(II). The absorption capacity of HNTs-PHT and HNTs-BP toward Hg(II) is

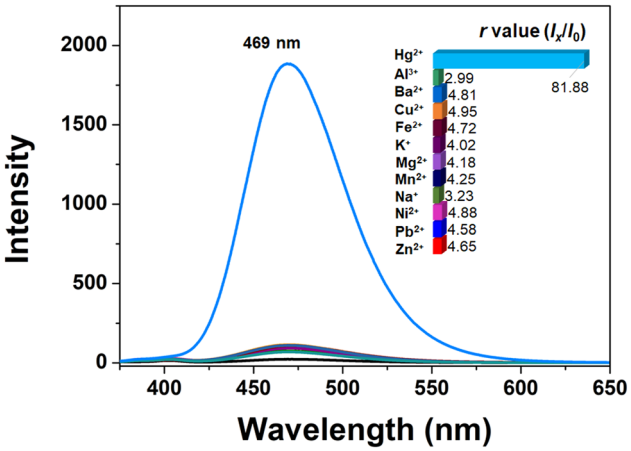

Figure 5: Fluorescence spectra of HNTs-PHT in aqueous solution ([*c*] = 1.0 mg/mL) with the addition of Hg^{2+}, Zn^{2+}, Pb^{2+}, Ni^{+}, Na^{+}, Mn^{2+}, Mg^{2+}, K^{+}, Fe^{2+}, Cu^{2+}, Ba^{2+} and Al^{3+} (the concentration of each ion is equal to 1×10^{-5} M).

calculated as ca. 110 and 95 mg/g. HNTs-PHT shows a higher absorption capacity than that of HNTs-NP. Otherwise, the dynamic adsorption behaviors of HNTs-PHT and HNTs-BP displayed distinct differences. The interaction of HNTs-based chemosensors and Hg(II) was investigated based on a turbidimetric assay method, which is widely used to evaluate the interactions of carbohydrates with proteins in the literature [58]. Plots of absorbance at 550 nm *vs* the time after the addition of Hg(II) were recorded and are shown in Figure S22. A completely different behavior can be tracked between HNTs-PHT and HNTs-BP, which should be caused by the difference in the formation between interparticle and intraparticle excimers. The intraparticle excimer cannot give rise to the changes in particle sizes. So, the chelation of HNTs-BP with Hg(II) cannot raise any significant changes in the absorbance values. The removal efficiency of HNTs-PHT toward Hg(II) in an aqueous solution was evaluated by adding 5.0 mg of HNTs-PHT into 1.0 mL of Hg(II) solution with different concentrations at 1×10^{-3}, 1×10^{-4} and 1×10^{-5} M. The removal efficiency follows a concertation-dependent manner, which was calculated ad 72, 85 and 91%, respectively.

As for HNTs-PHT, the formation of interparticle excimers makes Hg(II) ions serve as crosslinkers to aggregate the particles. As a result, a dramatic increase in absorbance values can be clearly found in HNTs-PHT after the

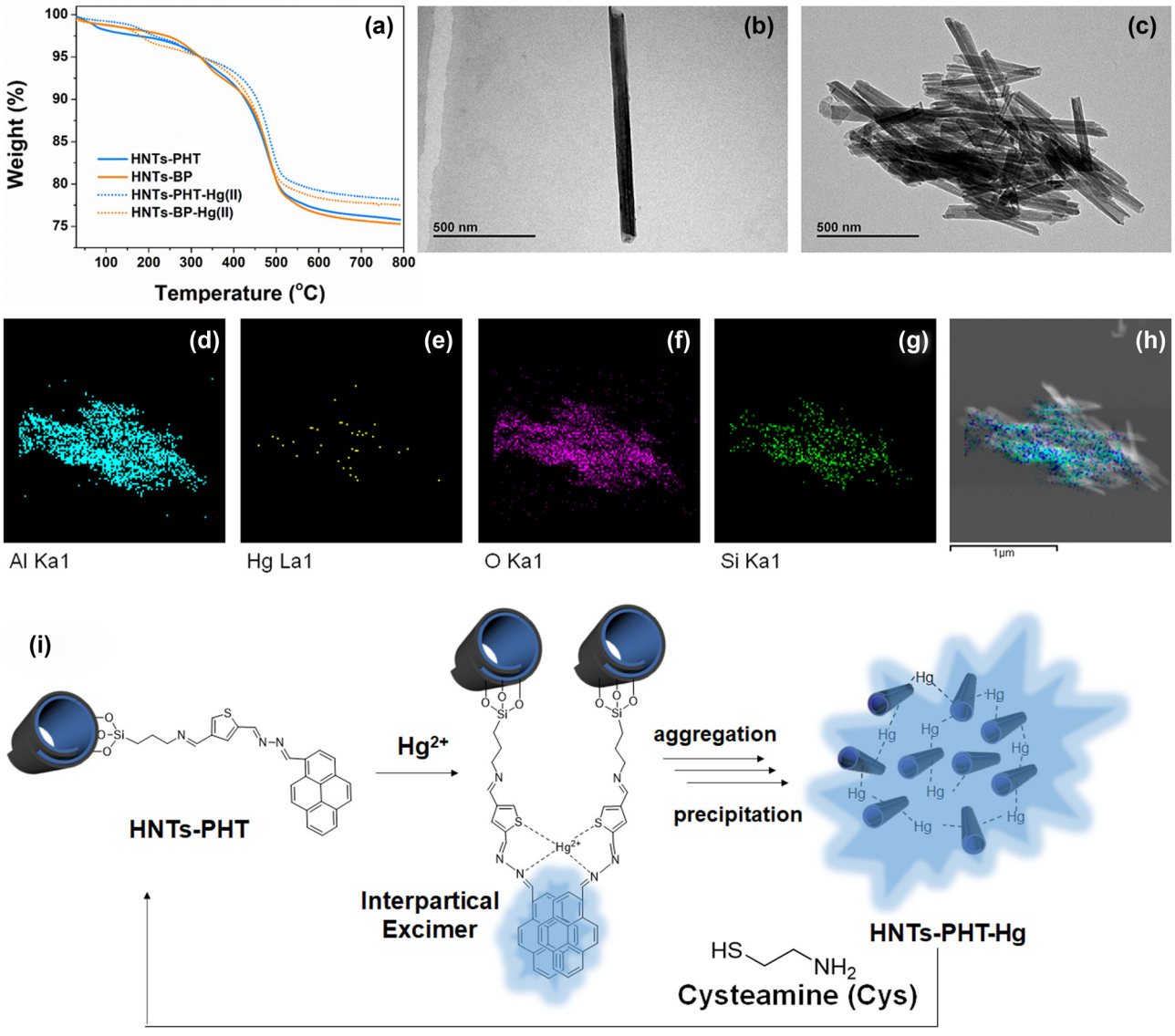

Figure 6: Absorption studies. [(a) TGA curves of HNTs-PHT, HNTs-BP, HNTs-PHT-Hg(II) and HNTs-BP-Hg(II); (b) TEM image of HNTs-PHT; (c) TEM image of HNTs-PHT-Hg(II); (d) EDS mapping of Al; (e) EDS mapping of Hg; (f) EDS mapping of O; (g) EDS mapping of Si; (h) mixture of the above-mentioned elements; and (i) aggregation and recycling mechanism for as-obtained HNTs-PHT-Hg(II).

formation of interparticle excimers, suggesting the formation of precipitations. Therefore, the separation of Hg(II) was achieved by a simple precipitation approach without power consumption, when using HNTs-PHT as the adsorbent. TEM observations were conducted to further characterize the as-obtained precipitations. Figure 6b reveals that the HNTs-PHT is the monodisperse cylindrical-shaped nanotube with an open-ended lumen. After chelating with Hg(II), the aggregates can be clearly observed in the TEM image (Figure 6c) of HNTs-PHT-Hg(II). The corresponding elemental maps displaced in Figure 6d–g illustrate the distribution of the detected elements in EDS analysis, including Al (blue in Figure 6d), Hg (yellow in Figure 6e), O (purple in Figure 6f) and Si (green in Figure 6g). The mixture of distribution of the abovementioned elements is shown in Figure 6h. The signals from Al, O and Si mappings show their elemental distribution in the nanotube-based aggregation, which is consistence with the chemical composition of HNTs. The presence of Hg and the highly coincided distribution with the Al, O and Si indicate that the aggregates should be caused by Hg(II) and thereby results in the macroscopic precipitations. Moreover, the Hg(II) ions can be dissociated from HNTs-PHT-Hg(II) with the addition of cysteamine, which endow HNTs-PHT a potential recyclable material for detecting and separating the Hg(II) (Figure 6i).

4 Conclusion

We have developed two types of HNTs-based chemosensors, HNTs-PHT and HNTs-BP, for simultaneously detecting and separating Hg(II) ions. The structural characterizations, including FTIR, solid-state NMR, XPS and TGA, demonstrated the successful modifications. The chemosensors have been covalently linked onto HNTs with good stability. Both HNTs-PHT and HNTs-BP are able to detect Hg(II) ions *via* a "turn on" behavior on fluorescence, in which HNTs-PHT can effectively restrict the solvent relaxation of π–π^* transition and make it a better detection tool in aqueous solution than HNTs-BP. The aqueous solution of HNTs-PHT displayed no emission behavior ($\Phi < 0.001$), while a significant increase in emission behavior ($\Phi = 0.07$) can be detected. HNTs-PHT shows highly specific, precise and sensitive responses to Hg(II) in an aqueous system as compared to the literature. Moreover, HNTs-PHT exhibited a high absorption capacity upon Hg(II) at ca. 110 mg/g, in which the Hg(II) ions serve as crosslinking agents to aggregate HNTs-PHT into macroscopical precipitations. The established simultaneously detecting and separating approach upon Hg(II) ions by HNTs-PHT gives a novel insight on dealing with a mercury pollution problem in water and widen the insight of environmental remediation.

NMR data, FTIR spectra, fluorescence spectra of HNTs-PB as a function of increasing water content, linear regression data and turbidity results are included in the Supporting information.

Funding information: This work was financially supported by the National Natural Science Foundation of China (Grant No. 22102045) and the Key Project from the Natural Science Foundation of Hebei Province (No. B2020201072).

Author contributions: The manuscript was written through contributions of all authors. Conceptualization: Y. Wu, X. Ba and H. Zhang; investigation and methodology: H. Fan, P. Jia and Z. Su; data curation: Y. Wu and H. Zhang; writing – original draft: H. Zhang; writing – review & editing: Y. Wu. All authors have accepted responsibility for the entire content of this manuscript and approved its submission.

Conflict of interest: The authors state no conflict of interest.

Reference

[1] Peng Y, Huang H, Zhang Y, Kang C, Chen S, Song L, et al. A versatile MOF-based trap for heavy metal ion capture and dispersion. Nat Commun. 2018;9(1):187.
[2] Tang Z, Qiu Z, Lu S, Shi X. Functionalized layered double hydroxide applied to heavy metal ions absorption: a review. Nanotechnol Rev. 2020;9(1):800–19.
[3] Xu J, Liu C, Hsu P-C, Zhao J, Wu T, Tang J, et al. Remediation of heavy metal contaminated soil by asymmetrical alternating current electrochemistry. Nat Commun. 2019;10(1):2440.
[4] Yuan X, Xue N, Han Z. A meta-analysis of heavy metals pollution in farmland and urban soils in China over the past 20 years. J Environ Sci. 2021;101:217–26.
[5] Khanam R, Kumar A, Nayak AK, Shahid M, Tripathi R, Vijayakumar S, et al. Metal(loid)s (As, Hg, Se, Pb and Cd) in paddy soil: Bioavailability and potential risk to human health. Sci Total Environ. 2020;699:134330.
[6] Cooke CA, Martinez-Cortizas A, Bindler R, Gustin MS. Environmental archives of atmospheric Hg deposition – a review. Sci Total Environ. 2020;709:134800.
[7] Dong L, Wang H, Huang Y, Zha J, Cheng H, Liu L, et al. γ-Fe_2O_3 decorated attapulgite composite modified with $CuCl_2$ as magnetically separable sorbents for Hg-0 removal from coal combustion flue gas. Chem Eng J. 2021;408:127888.
[8] Sadani K, Nag P, Mukherji S. LSPR based optical fiber sensor with chitosan capped gold nanoparticles on BSA for trace detection of Hg (II) in water, soil and food samples. Biosens Bioelectron. 2019;134:90–6.

[9] De Gregori I, Quiroz W, Pinochet H, Pannier F, Potin-Gautier M. Simultaneous speciation analysis of Sb(III), Sb(V) and $(CH_3)_3SbCl_2$ by high performance liquid chromatography-hydride generation-atomic fluorescence spectrometry detection (HPLC-HG-AFS): application to antimony speciation in sea water. J Chromatogr A. 2005;1091(1–2):94–101.
[10] Su X, Kushima A, Halliday C, Zhou J, Li J, Hatton TA. Electrochemically-mediated selective capture of heavy metal chromium and arsenic oxyanions from water. Nat Commun. 2018;9:4701.
[11] Sengupta P, Pramanik K, Sarkar P. Simultaneous detection of trace Pb(II), Cd(II) and Hg(II) by anodic stripping analyses with glassy carbon electrode modified by solid phase synthesized iron-aluminate nano particles. Sens Actuators B Chem. 2021;329:129052.
[12] Haldar U, Lee H-i. BODIPY-derived polymeric chemosensor appended with thiosemicarbazone units for the simultaneous detection and separation of Hg(II) ions in pure aqueous media. ACS Appl Mater Interfaces. 2019;11(14):13685–93.
[13] Zhou L, Lin Y, Huang Z, Ren J, Qu X. Carbon nanodots as fluorescence probes for rapid, sensitive, and label-free detection of Hg^{2+} and biothiols in complex matrices. Chem Commun. 2012;48(8):1147–9.
[14] Gale PA, Caltagirone C. Anion sensing by small molecules and molecular ensembles. Chem Soc Rev. 2015;44(13):4212–27.
[15] Yuan W, Lu P, Chen S, Lam JWY, Wang Z, Liu Y, et al. Changing the behavior of chromophores from aggregation-caused quenching to aggregation-induced emission: development of highly efficient light emitters in the solid state. Adv Mater. 2010;22(19):2159–63.
[16] Wang D, Tang B. Aggregation-induced emission luminogens for activity-based sensing. Acc Chem Res. 2019;52(9):2559–70.
[17] Aathimanikandan SV, Savariar EN, Thayumanavan S. Temperature-sensitive dendritic micelles. J Am Chem Soc. 2005;127(42):14922–29.
[18] Nakano M, Fukuda M, Kudo T, Miyazaki M, Wada Y, Matsuzaki N, et al. Static and dynamic properties of phospholipid bilayer nanodiscs. J Am Chem Soc. 2009;131(23):8308–12.
[19] Awual MR. Novel nanocomposite materials for efficient and selective mercury ions capturing from wastewater. Chem Eng J. 2017;307:456–65.
[20] Abbas K, Znad H, Awual MR. A ligand anchored conjugate adsorbent for effective mercury(II) detection and removal from aqueous media. Chem Eng J. 2018;334:432–43.
[21] Liu J, Hui D, Lau D. Two-dimensional nanomaterial-based polymer composites: fundamentals and applications. Nanotechnol Rev. 2022;11(1):770–92.
[22] Glotov A, Vutolkina A, Pimerzin A, Vinokurov V, Lvov Y. Clay nanotube-metal core/shell catalysts for hydroprocesses. Chem Soc Rev. 2021;50(16):9240–77.
[23] Cheng C, Song W, Zhao Q, Zhang H. Halloysite nanotubes in polymer science: purification, characterization, modification and applications. Nanotechnol Rev. 2020;9(1):323–44.
[24] Zhao S, Yuan Y, Yu Q, Niu B, Liao J, Guo Z, et al. A dual-surface amidoximated halloysite nanotube for high-efficiency economical uranium extraction from seawater. Angew Chem Int Ed. 2019;58(42):14979–85.
[25] Pierchala MK, Kadumudi FB, Mehrali M, Zsurzsan T-G, Kempen PJ, Serdeczny MP, et al. Soft electronic materials with combinatorial properties generated via mussel-inspired chemistry and halloysite nanotube reinforcement. ACS Nano. 2021;15(6):9531–49.
[26] Feng X, Liu D, Yan B, Shao M, Hao Z, Yuan G, et al. Highly active $PdO/Mn_3O_4/CeO_2$ nanocomposites supported on one dimensional halloysite nanotubes for photoassisted thermal catalytic methane combustion. Angew Chem Int Ed. 2021;60(34):18552–6.
[27] Fakhrullina G, Khakimova E, Akhatova F, Lazzara G, Parisi F, Fakhrullin R. Selective antimicrobial effects of curcumin@halloysite nanoformulation: a *Caenorhabditis Elegans* study. ACS Appl Mater Interfaces. 2019;11(26):23050–64.
[28] Luo X, Zhang J, Wu Y-P, Yang X, Kuang X-P, Li W-X, et al. Multifunctional $HNT@Fe_3O_4$@PPy@DOX nanoplatform for effective chemo-photothermal combination therapy of breast cancer with MR imaging. ACS Biomater Sci Eng. 2020;6(6):3361–74.
[29] Long Z, Wu Y-P, Gao H-Y, Zhang J, Ou X, He R-R, et al. In vitro and in vivo toxicity evaluation of halloysite nanotubes. J Mater Chem B. 2018;6(44):7204–16.
[30] Lisuzzo L, Cavallaro G, Milioto S, Lazzara G. Halloysite nanotubes as nanoreactors for heterogeneous micellar catalysis. J Colloid Interface Sci. 2022;608:424–34.
[31] Lvov Y, Shchukin D, Mohwald H, Price R. Halloysite clay nanotubes for controlled release of protective agents. ACS Nano. 2008;2(5):814–20.
[32] Lisuzzo L, Cavallaro G, Milioto S, Lazzara G. Halloysite nanotubes filled with MgO for paper reinforcement and deacidification. Appl Clay Sci. 2021;213:106231.
[33] Yu L, Wang H, Zhang Y, Zhang B, Liu J. Recent advances in halloysite nanotube derived composites for water treatment. Environ Sci Nano. 2016;3(1):28–44.
[34] Zhang Y, Wang H, Liu J, Hou J, Zhang Y. Enzyme-embedded metal-organic framework membranes on polymeric substrates for efficient CO_2 capture. J Mater Chem A. 2017;5(37):19954–62.
[35] Zahidah KA, Kakooei S, Ismail MC, Raja PB. Halloysite nanotubes as nanocontainer for smart coating application: a review. Prog Org Coat. 2017;111:175–85.
[36] Wei Y, Yuan P, Liu D, Losic D, Tan D, Chen F, et al. Activation of natural halloysite nanotubes by introducing lanthanum oxycarbonate nanoparticles via co-calcination for outstanding phosphate removal. Chem Commun. 2019;55(14):2110–3.
[37] Zhang J, Luo X, Wu Y, Wu F, Li Y, He R, et al. Rod in Tube: a novel nanoplatform for highly effective chemo-photothermal combination therapy toward breast cancer. ACS Appl Mater Interfaces. 2019;11(4):3690–703.
[38] Wu S, Qiu M, Guo B, Zhang L, Lvov YM. Nanodot-loaded clay nanotubes as green and sustained radical scavengers for elastomer. ACS Sustain Chem Eng. 2017;5(2):1775–83.
[39] Li L, Zhou Y, Gao R, Liu X, Du H, Zhang J, et al. Naturally occurring nanotube with surface modification as biocompatible, target-specific nanocarrier for cancer phototherapy. Biomaterials. 2019;190–191:86–96.
[40] Fan L, Zhang J, Wang A. In situ generation of sodium alginate/hydroxyapatite/halloysite nanotubes nanocomposite hydrogel beads as drug-controlled release matrices. J Mater Chem B. 2013;1(45):6261–70.

[41] Ouyang J, Zhao Z, Yang H, Zhang Y, Tang A. Large-scale synthesis of sub-micro sized halloysite-composed cza with enhanced catalysis performances. Appl Clay Sci. 2018;152:221–9.
[42] Sadjadi S, Lazzara G, Malmir M, Heravi MM. Pd nanoparticles immobilized on the poly-dopamine decorated halloysite nanotubes hybridized with N-doped porous carbon monolayer: a versatile catalyst for promoting Pd catalyzed reactions. J Catal. 2018;366:245–57.
[43] Sidorenko AY, Kravtsova AV, Aho A, Heinmaa I, Warna J, Pazniak H, et al. Highly selective Prins reaction over acid-modified halloysite nanotubes for synthesis of isopulegol-derived 2H-chromene compounds. J Catal. 2019;374:360–77.
[44] Cao X, Sun Y, Sun Y, Xie D, Li H, Liu M. Conductive halloysite clay nanotubes for high performance sodium ion battery cathode. Appl Clay Sci. 2021;213:106265.
[45] Ghanei-Motlagh M, Taher MA. A novel electrochemical sensor based on silver/halloysite nanotube/molybdenum disulfide nanocomposite for efficient nitrite sensing. Biosens Bioelectron. 2018;109:279–85.
[46] Shao L, Wang X, Yang B, Wang Q, Tian Q, Ji Z, et al. A highly sensitive ascorbic acid sensor based on hierarchical polyaniline coated halloysite nanotubes prepared by electrophoretic deposition. Electrochim Acta. 2017;255:286–97.
[47] Feng Y, Luo X, Wu F, Liu H, Liang E, He R, et al. Systematic studies on blood coagulation mechanisms of halloysite nanotubes-coated PET dressing as superior topical hemostatic agent. Chem Eng J. 2022;428:132049.
[48] Cheng C, Gao Y, Song W, Zhao Q, Zhang H, Zhang H. Halloysite nanotube-based H_2O_2-responsive drug delivery system with a turn on effect on fluorescence for real-time monitoring. Chem Eng J. 2020;380:122474.
[49] Zhao Q, Jiang H, Tang B, Wu Y, Ba X, Zhang H. Chemosensor-anchored halloysite nanotubes for detection and removal of hypochlorite in water. ACS Appl Nano Mater. 2021;4(7):7435–42.
[50] Su Z, Zhang H, Gao Y, Huo L, Wu Y, Ba X. Coumarin-anchored halloysite nanotubes for highly selective detection and removal of Zn(II). Chem Eng J. 2020;393:124695.
[51] Liu F, Bai L, Zhang H, Song H, Hu L, Wu Y, et al. Smart H_2O_2-responsive drug delivery system made by halloysite nanotubes and carbohydrate polymers. ACS Appl Mater Interfaces. 2017;9(37):31626–33.
[52] Sarkar S, Roy S, Saha RN, Panja SS. Thiophene appended dual fluorescent sensor for detection of Hg^{2+} and cysteamine. J Fluoresc. 2018;28(1):427–37.
[53] Zhou Y, Zhu C, Gao X, You X, Yao C. Hg^{2+}-selective ratiometric and “Off-On” chemosensor based on the azadiene-pyrene derivative. Org Lett. 2010;12(11):2566–9.
[54] Awual MR, Hasan MM. A ligand based innovative composite material for selective lead(II) capturing from wastewater. J Mol Liq. 2019;294:111679.
[55] Islam MA, Angove MJ, Morton DW, Pramanik BK, Awual MR. A mechanistic approach of chromium (VI) adsorption onto manganese oxides and boehmite. J Environ Chem Eng. 2020;8(2):103515.
[56] Awual MR. An efficient composite material for selective lead(II) monitoring and removal from wastewater. J Environ Chem Eng. 2019;7(3):103087.
[57] Awual MR. Novel ligand functionalized composite material for efficient copper(II) capturing from wastewater sample. Compos Part B Eng. 2019;172:387–96.
[58] Chen Y, Chen G, Stenzel MH. Synthesis and lectin recognition of glyco star polymers prepared by “clicking” thiocarbohydrates onto a reactive scaffold. Macromolecules. 2010;43(19):8109–14.